www.sciencemag.org/cgi/content/full/345/6200/1038/DC1

Supplementary Materials for

Strength of stick-slip and creeping subduction megathrusts from heat flow observations

Xiang Gao and Kelin Wang*

*Corresponding author. E-mail: kwang@nrcan.gc.ca

Published 29 August 2014, *Science* **345**, 1038 (2014)
DOI: 10.1126/science.1255487

This PDF file includes:

Materials and Methods

Finite Element Model

We use a steady-state two-dimensional isoparametric finite element model similar to that of Wada and Wang (*31*). The model consists of an overriding and subducting plate with prescribed motion and a viscous mantle wedge with a temperature- and stress-dependent rheology. We use quadratic nine-node elements for temperature and velocity calculation and compatible bi-linear four-node elements for pressure calculation. Element size ranges from ~2.5 m to ~7.5 km in the largest dimension. Boundary conditions are assigned in the same way as in (*31*).

We employ a newly developed line-element technique to represent the subduction interface. Stress and rheology of the interface shear zone are analytically integrated over the thickness of the shear zone to yield properties of the line element. Compared to the viscous-layer (*31*) and differential-motion (*32*) methods, the new technique can handle any shear-zone thickness and rheology, more accurately calculates stress and heat dissipation, and is devoid of numerical instability. Following (*31*), we assume the coupling of the slab and mantle wedge material occurs at depths greater than 75 km, although our fault heat dissipation results are insensitive to the precise value of the coupling depth.

The model for each subduction zone is developed along a representative corridor oriented in the margin-normal direction. The deeper plate interface geometry for Japan Trench (Fig. 2A) is based on the Slab1.0 model (*33*), and the shallow part is based on the seismic imaging results in (*34*). The interface geometry for Northern Hikurangi (Fig. 2B) is from (*35*). Sources of interface geometry for other subduction zones are given in the captions of Figs. S1 through S7. Applying the GDH1 plate cooling model (*36*), we assume a slab thickness of 95 km, but this parameter is unimportant because the age-dependent thermal structure of the incoming plate is advected downdip by the plate to control the thermal state of the subduction system. The Moho depth of the overriding plate at continental margins is in the range of 30-40 km (Figs. 2, S1–S7). At ocean-ocean margins, the Moho depth is assumed to be 12-13 km based on seismic studies at the Lzu-Bonin-Mariana margin [*e.g.*, (*37*)].

The subduction rate V is the speed of the slab with respect to the overriding forearc. In some cases, it is the same as the convergence rate between to two converging plates and can be obtained directly from the global plate model (*38*) (Table S2). In other cases, the forearc sliver moves relative to the rest of the upper plate such that the slab motion with respect to the forearc is not as oblique as with respect to most of the upper plate. In the latter situation, the subduction rate is obtained from regional tectonic studies (Table S2). Our 2D model employs the margin-normal component of the subduction rate. Obviously, the calculation of heat dissipation must involve the full subduction rate.

Model Parameters

We use typical values of thermal conductivity and volumetric thermal capacity (specific heat times density) for various rock units (Table S1). Errors in these parameters contribute very little to uncertainties in μ' as compared to those of radiogenic heat production of forearc rocks. Assuming radiogenic heat production is mainly in a 15 km thick upper crust, an error of ±0.2 μW m^{-3} translates to an error of ±3 mW m^{-2} in the

predicted surface heat flow. The resultant uncertainty in μ' inferred from heat flow measurements is around 0.01, with small variations inversely dependent on the subduction rate. The uncertainties in heat production can affect the estimate of frictional heating in individual subduction zones, but these random errors are extremely unlikely to introduce a systematic bias to result in a trend as shown in Fig. 4.

Because of naturally heterogeneous distribution of radiogenic elements, heat production values measured on rock samples show very large variations even for an otherwise uniform rock formation. We use average values of these measurements at different subduction zones for our modeling (Table S1). Uncertainties for these average values should be much smaller than the spread of the measured values and are assumed to be about 0.1-0.3 μW m^{-3}. For Japan Trench and Nankai forearcs, the majority of the measured values of granitic upper crust rock samples are between 1.5 and 2.2 μW m^{-3}, with an average 1.8 μW m^{-3}, and values for most of the offshore sediments are around 1.5 μW m^{-3} (*39, 40, 41*). Given that much of the accretionary prism sediments were derived from granitic rocks on land, a heat production value of 1.5 μW m^{-3} is an underestimate which may cause some overestimation of μ' at Nankai. For northern Hikurangi, heat production values measured on many core samples from industrial wells are mostly between 1.07 and 1.95μW m^{-3}, with an average value 1.7 μW m^{-3} (*42*). For the Chile forearc, the average values of plutonic rocks and sediments are reported to be 0.9 and 0.8, respectively (*43*). For northern Cascadia, the continental basement is composed mainly of mafic materials which have very low concentrations of radiogenic elements, and reported measurement values are mostly between 0.6 and 0.8 μW m^{-3} (*44*). Following (*45*) and (*46*), we use heat production rates that increase from 0.2 at the deformation front to 1.3 μW m^{-3} near the arc. At Kermadec, the upper plate is oceanic which has with very low heat production. We use values reported for the Tonga forearc (*47*). The values range between 0.05 and 0.1 μW m^{-3} with an average 0.08 μW m^{-3}. For northern Manila Trench, we assume 0.02 μW m^{-3} for the basement rocks but 1.3±0.3 μW m^{-3} for the overlying sediments which have been derived mainly from continental China and Taiwan. For Sumatra and Kamchatka, where measurements are not available, we assume the typical continental value 1.3±0.3 μW m^{-3} for the upper crust and sediments (*31*).

Assuming radiogenic heat production is mainly in a 15 km thick upper crust, an error of ±0.2 μW m^{-3} translates to an error of ±3 mW m^{-2} in the predicted surface heat flow. The resultant uncertainty in μ' inferred from heat flow measurements is around 0.01, with small variations inversely dependent on the subduction rate. The uncertainties in heat production can affect the estimate of frictional heating in individual subduction zones, but these random errors are extremely unlikely to introduce a systematic bias to result in a trend as shown in Fig. 4.

One process we do not consider is possible vigorous hydrothermal circulation within the subducted crust as proposed for one part of the Nankai subduction zone (*48*), some 200 km from our model transect, to explain anomalously high heat flows observed at the trench accompanied with a sharp landward decrease. This effect can reduce surface heat flow landward of the trench and, if not properly accounted for, lead to an underestimate of μ'. This effect may be important for very young subducting oceanic crust if its permeability is maintained extremely high by local geological conditions (*48*). In the area of our Nankai model transect where the age of the subducting plate is about 20 Ma, this effect is negligible (*49*). The subducting crust for most of the other subduction zones in

Fig. 4 is much older. At northern Cascadia, the subducting crust is very young, but there is no evidence for anomalously high heat flow at the trench.

Heat Dissipation Along the Megathrust

The rate of heat dissipation per unit area q is the product of fault shear stress τ and fault slip rate V. The shallow part of the fault is governed by the static friction law

$$\tau^F = \mu(\sigma_n - P) = \mu(1-\lambda)\sigma_n = \mu'\sigma_n \quad \text{(S1)}$$

where P is pore fluid pressure, λ is the ratio of fluid pressure to normal stress (approximately the lithostatic stress), μ' is normally referred to as the effective coefficient of friction but is called the apparent coefficient of friction here because of the complex nature of τ and V in stick-slip motion as discussed in the main text (Fig. 3). The deeper part of the fault is assumed to follow the flow law (*14*)

$$\tau^V = (C\tau^{r-n})^{-1/n}\left(\frac{V}{w}\right)^{1/n} exp\left(\frac{E}{nRT}\right) \quad \text{(S2)}$$

where C, r, and n are experimentally determined parameters, w is the thickness of shear zone that accommodates fault slip, E is the activation enthalpy, R is the universal gas constant, and T is absolute temperature.

There is no established method to define the rheology and thickness of the viscous shear zone and how they evolve with increasing depth. We use parameters for wet granite (*50*) with a thickness of 500 m to represent the shear zone. Although the use of granite is somewhat relevant because of the presence of upper plate crustal material and subducted sediments, we do not attach much significance to these parameters because of the trade-off between flow-law parameters and shear zone thickness. For the purpose of this work, it is the frictional segment of the megathrust that is of primary interest.

In previous thermal models, downdip transition along the subduction interface from the shallow frictional slip to deeper viscous shearing with increasing temperature is abrupt. Here, we invoke a parameterization based on laboratory experiments (*14*). In this approach, the strength of the fault is

$$\tau = \tau^V \tanh(\tau^F/\tau^V) \quad \text{(S3)}$$

The resultant gradual frictional-viscous transition accounts for the semi-brittle behavior observed in nature (*14*).

Supplementary Text

Table S2 summarizes main geographic and tectonic parameters for the subduction zones included in Fig. 4 except Costa Rica for which the estimate of μ' is averaged from previous thermal modeling results (*51, 52, 53*). Here we provide details on the heat flow data and comparison of model results with previous studies. If uncertainties in the heat flow data were not provided in original references or database, we assume a typical value of 10 mW m^{-2}. The uncertainties represent errors in field and laboratory measurements as well as in corrections made for various perturbing factors. However, it is common that the scatter of heat flow values between neighboring sites is larger than estimated uncertainties in individual measurements, reflecting natural variations due to various known or unknown physical processes. It is neither simple nor meaningful to design statistical measures of model fit to the heat flow data. Thus, as in all other thermal modeling efforts, the choice of preferred models is based on visual inspection of results,

influenced by the authors' understanding of the physical process and of the limits of the theoretical model used.

Northern Hikurangi

Townend et al. (*54*) derived marine heat flow values from gas hydrate Bottom-Simulating-Reflector (BSR) data, with reported uncertainties 10 mW m^{-2}, and corrected for the effects of late Neogene sedimentation. Pandey (*42*) and Field et al. (*55*) had calculated heat flows using bottom-hole temperature measurements in terrestrial boreholes and average conductivities of core samples. We re-examined the original bottom-hole temperature data and classified the borehole heat flow data into the following three groups. In group C1, the downhole temperatures are densely spaced, are well-aligned to define a gradient, and can be upward extrapolated to the average ground surface temperature (~15℃). The C2 group show similar characteristics to the C1 group except for more sparsely spaced temperature measurements. In group C3, there are different indicators of problems, such as the upward extrapolation of borehole temperatures being inconsistent with the average surface temperature, signs of fluid flow perturbing borehole temperatures, or only one temperature measurement in the hole. The C1, C2, and C3 heat flow values are assigned errors ±5, ±15, and ±25 mW m^{-2}, respectively (Fig. 2B). The terrestrial heat flow data obtained by Studt et al. (*56*) are not included in our study because the depths of measurements were very shallow (< 150 m) and the measured temperatures often show signs of fluid perturbation.

Several thermal models have been constructed for Northern Hikurangi using these heat flow data as constraints (*31, 57, 58*). McCaffrey et al. (*57*) applied the analytical solution of Molnar and England (*59*) and favored a shear stress 20 MPa along the fault. Fagereng and Ellis (*58*) concluded that the real value of μ' ranged between 0.03 and 0.36. Wada and Wang (*31*) assumed a μ' value of 0.03. In our model, a μ' value of 0.13 best agrees with the heat flow data (Fig. 2B). This value yields 20 MPa fault stress 30 km from the trench but much higher stress farther landward (Fig. 2B). The value of 0.03 used by Wada and Wang's (*31*) under-predicts the majority of the BSR heat flow values by about 10 mW m^{-2} and even worse for the average land values. Increasing the value of μ' by 0.1 better fits the heat flows (Fig. 2B). The slight difference between the distribution of projected heat flow data in Fig. 2B and that of Wada and Wang (*31*) is due to different model profile orientations, with ours being more perpendicular to the trench (Fig. 1B).

Manila Trench

Chi and Reed (*60*) obtained more than 1000 BSR heat flow values along seismic lines south of Taiwan and divided them into three quality categories (Q1, Q2, and Q3) (*60*) (Fig. S1A). Shyu et al. (*61, 62*) made over 40 probe heat flow measurements (Fig. S1A). Although the probe values are too far north to be used in our modeling, they serve to validate the BSR values. The average probe heat flow is 16% higher than that estimated from BSR in their overlapping area (*62*). If this reflects a systematic bias in the BSR estimates, the actual heat flow might be slightly higher than shown in Fig. S1B, and hence the preferred μ' value should also be slightly higher.

Chi and Reed (*60*) applied an analytical solution (*59*) assuming a planar plate interface. The heat flow data they chose to constrain the model were from a 10 km wide corridor along their model profile and all were of the lowest quality (Q3). The average

value along that corridor is 10-15 mW m^{-2} lower than that along a 40 km wide corridor along the same profile which includes many Q2 level data. Consequently, they did not find frictional heating necessary in their modeling. Our preferred μ' value of about 0.09 is constrained by the Q2 heat flow data from this wider corridor (Fig. S1). The subducting seafloor at the Manila Trench was considered extremely rough by Wang and Bilek (*2*), but shown as being rough in Table S2. This is because large amount of sediments made the roughness of the area covered by the heat flow measurements (*60*) less extreme. As explained by Wang and Bilek (*2*), the igneous basement in this area is very rugged, with seamounts often penetrating the sediment cover.

Kermadec

von Herzen *et al*. (*63*) acquired densely spaced heat flow measurements using 4-m long heat flow probes along two margin-normal profiles at 1500 – 6000 m water depths (Fig. S2A). The penetration depth of the deepest usable thermal sensor is mostly in the range of 2 - 3 m below seafloor. Thermal conductivity values were determined in situ and compared with laboratory measurements on piston cores. von Herzen *et al.* (*63*) explained that the largest uncertainties in the heat flow data arise from recent bottom water temperature variations, and they made a correction for this effect by approximating the variations at each site with a step function. The large scatter of heat flow values near the western end of the profiles (Fig. S2B) may reflect hydrothermal activity near the volcanic front.

von Herzen *et al*. (*63*) used an analytical solution (*59*) assuming a planar subduction interface. To explain the heat flow data, they invoked frictional heating along the interface due to either a uniform shear stress of ~40 ±17 MPa or stress increasing linearly at ~0.5 ± 0.2 MPa/km with distance from the trench. The linear increase approximately corresponds to an apparent friction coefficient of 0.063 assumed 2750 kg/m^3 for the average density of overriding rocks. Our finite element model predicts a similar value of about 0.07 (Fig. S2B). We consider the incoming seafloor rough because it is decorated with a number of seamounts that are 2-3 km tall.

Nankai

A large amount of heat flow data have been collected at the Nankai margin (Fig. S3) (*49*). Heat flow probe values (grey circles in Fig. S3) show a large scatter which is caused by near-surface fluid activities in the accretionary prism (*64*). There are significant bottom water temperature variations at shallow water depths, and the few extremely high probe values about 50-100 km from the trench (red circles) may be due to this effect. Values corrected for this effect based on in situ long-term temperature monitoring (Fig. S3) are considered more reliable (*64*). Integrated Ocean Drilling Program (IODP) borehole values and BSR values are less affected by near-surface fluid flow and bottom temperature variations.

Many thermal models have been developed using the heat flow data as constraints (*31, 48, 64-68*). In the published models, the apparent coefficient of friction are in the range of 0 - 0.05. The preferred value of 0.03 in our new model is consistent with previous findings, although lower values are also acceptable. A value of 0.06 over-predicts most of the IODP and BSR heat flow values. The time-dependent Nankai model

by Wang *et al*. (*65*) took into consideration the age history of the subducting plate. Here for simplicity we follow all other published Nankai thermal models to use a steady-state model. The steady-state model does not account for the fact that the present thermal regime has evolved from a warmer past when the incoming plate was younger. It therefore tends to require greater frictional heating to compensate for the missing heat. For this reason, the μ' value of 0.03 should be considered an upper limit.

Kamchatka

Tanaka *et al*. (*69*) compiled probe and borehole heat flow data for the Kamchatka margin (Fig. S4) collected over three decades. Heat flow values in the shallow sea areas have a large scatter, likely due to bottom temperature variations similar to the situation at Nankai (*64*). Values in the deep water provide better constraints. The relatively uniform subducting slab geometry and subduction rate along strike encourage us to project widely distributed heat flow measurements onto our model profile. Our preferred value 0.03 for μ' is the same as what was used by Wada and Wang (*31*) in an earlier model. The value 0.09 over-predicts all the deep-water heat flow values and half of the shallow-water values (Fig. S4B). We considered this value an upper limit. Further increase in μ' does not produce higher heat flow in the shallow sea area because the stress in the deeper part of the fault becomes lower due to the onset of ductile creep (Fig. S4B).

Northern Cascadia

Different types of heat flow measurements including BSRs, probes, shelf wells, land boreholes and an ODP borehole have been collected and have been described in great detail in previous publications (*44, 70, 71*) (Fig. S5). The BSR values have been corrected for the effect of sediment thickening and fluid expulsion because the Cascadia accretionary prism grew rapidly seaward over the past few million years (*45*). Several thermal models have been developed for northern Cascadia (*45, 46, 72*), with μ' ranging from 0 to 0.03. We prefer a value of 0.02, although the value of zero or 0.06 is also acceptable.

Japan Trench

In and around Japan, heat flow data based on different measurement methods were compiled in (*69*). The heat flow values along the Japan Trench forearc show a high degree of consistency which is considered to reflect on the good quality of the measurements as well as the rather uniform subduction geometry along strike (Figs. 1A and 2A).

Many thermal models have been developed using these heat flow data as constraints (*31, 66, 73, 74*). In all the former models, frictional stress along the subduction fault was very low. Furukawa and Uyeda (*73*) concluded that the frictional stress should be lower than 20 MPa. Peacock and Wang (*66*) assumed a constant frictional stress 20 MPa along the subduction fault down to 70 km. We prefer a μ' value of 0.025, which translates to a frictional stress 12.8 MPa at 20 km depth and 26.7 MPa at 40 km depth (Fig. 2A). This value is similar to the value of 0.03 used by Wada and Wang (*31*) and Kimura et al. (*74*).

Sumatra

At the Sumatra margin (Fig. S6A), all the available heat flow data were collected in

the marine environment, as described in (*75*). Early probe heat flow values can be found in the Global Heat Flow Database (GHFD). More recent probe values were acquired during two scientific cruises following the 2004 earthquake. BSR heat flow values derived during the R/V Sonne cruise 189 show large scattering ranging 30–60 mW m^{-2} (*76*). Most of the probe values collected during the same cruise are extremely high, possibly because the measurement sites were positioned on faults hosting active hydrothermal circulation (*76*). Probe values obtained during the other cruise, the Marion Dufresne Aftershocks Cruise, and the BSR heat flow from R/V Sonne cruise 189 are considered more reliable.

Previous numerical thermal models employed a very low frictional stress along the Sumatra megathrust (*31, 75, 77*). Hippchen and Hyndman (*77*) suggested μ' values of 0-0.04. Wada and Wang (*31*) assumed a value of 0.03. Klingelhoefer et al. (*75*) employed an effective shear stress of 10 MPa on the subduction interface to about 40 km depth. Our preferred value of 0.03 is consistent with the earlier works. A value 0.08 over-predicts most of the heat flow values except the abnormally high values possibly associated with hydrothermal circulation (Fig. S6B).

South-Central Chile

Many BSR, probe, and ODP borehole heat flows were acquired along the Chile margin (*43, 78, 79*) (Fig. S7A). All the measurements were made in deep water far offshore and can only provide heat flow constraints within 50 km of the trench (for interface depths < 16 km). Two ODP boreholes (Leg 202) produced some of the best-quality heat flow data. The surrounding BSR and probe heat flows are consistent with the borehole values. To the north of the borehole sites, there are some abnormally high probe values which may have been affected by fluid flow (*79*).

In a thermal model based on an analytical solution (*59*) assuming a planar subduction fault, Grevemeyer *et al*. (*43*) assigned a very low shear stress < 10 MPa along the subduction megathrust in order to fit the heat flow observations. In a finite-element thermal model, Völker *et al*. (*80*) found that the heat flow observations could be satisfied even without invoking frictional heating. Our preferred μ' value of 0.03 is consistent with the previous studies, although a value of 0.0 or 0.06 can also marginally fit the limited data.

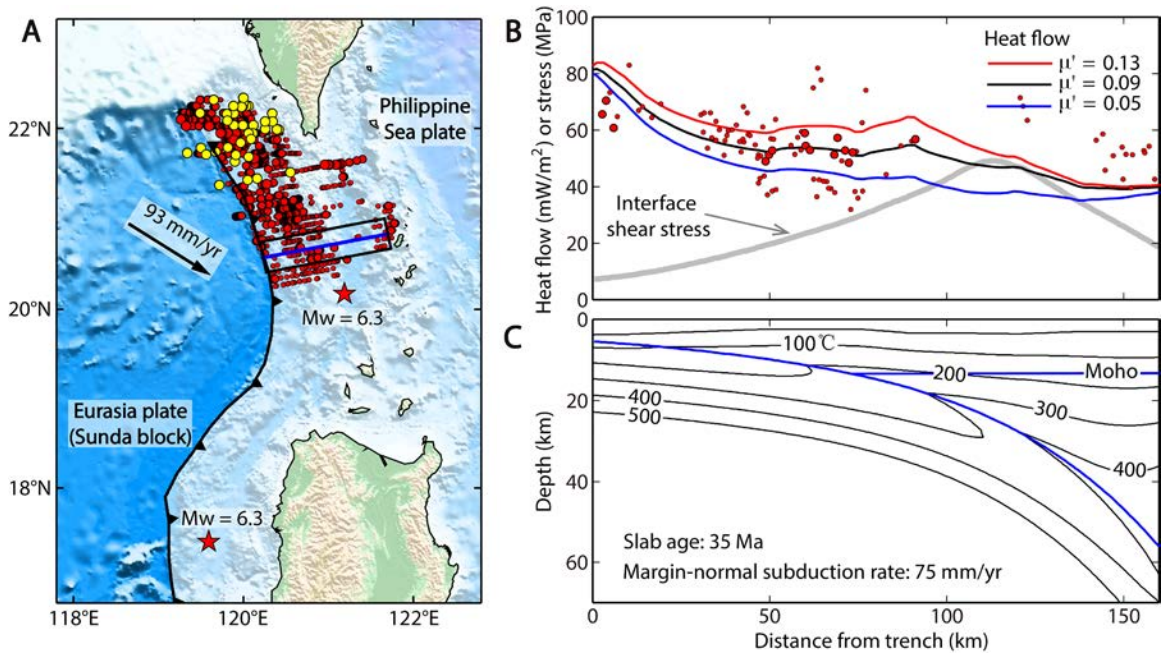

Fig. S1.

Manila Trench model. (A) Tectonic setting. Red circles are BSR heat flow sites. Three sizes of the circles indicate the three quality classes of heat values Q1, Q2, and Q3, with the largest representing the highest quality (Q1) (*60*). Yellow circles are probe heat flow sites (*61*, *62*). Heat flow data shown in (B) are from the corridor (black box) along the model profile (thick blue line). Red star indicates epicenter of largest recorded thrust earthquakes at this margin (Table S2). (B) Observed (symbols) and model-predicted (lines) heat flow values and model interface shear stress. Larger and smaller circles indicate class Q2 and Q3 BSR heat flow data, respectively. (C) Thermal structure. The slab geometry is obtained by combining a seismic tomography model (*81*), a gravity model (*82*), and earthquake distribution (*83*).

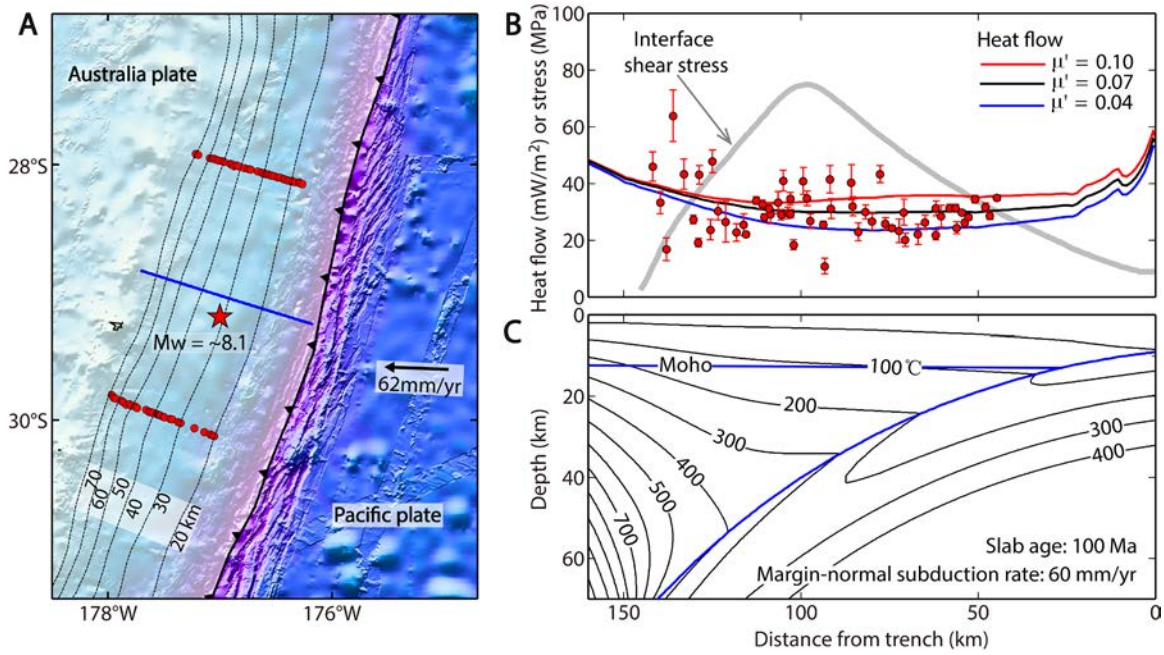

Fig. S2

Kermadec model. (A) Tectonic setting. Red circles are heat flow sites (*63*). Red star indicates epicenter of largest recorded thrust earthquake at this segment of the margin (Table S2). Plate interface depths (black contour lines) are from (*33*). Thick blue line indicates model profile. (B) Observed (symbol) and the model-predicted (lines) heat flow and model interface shear stress. (C) Thermal structure. Interface geometry is the same as in (A).

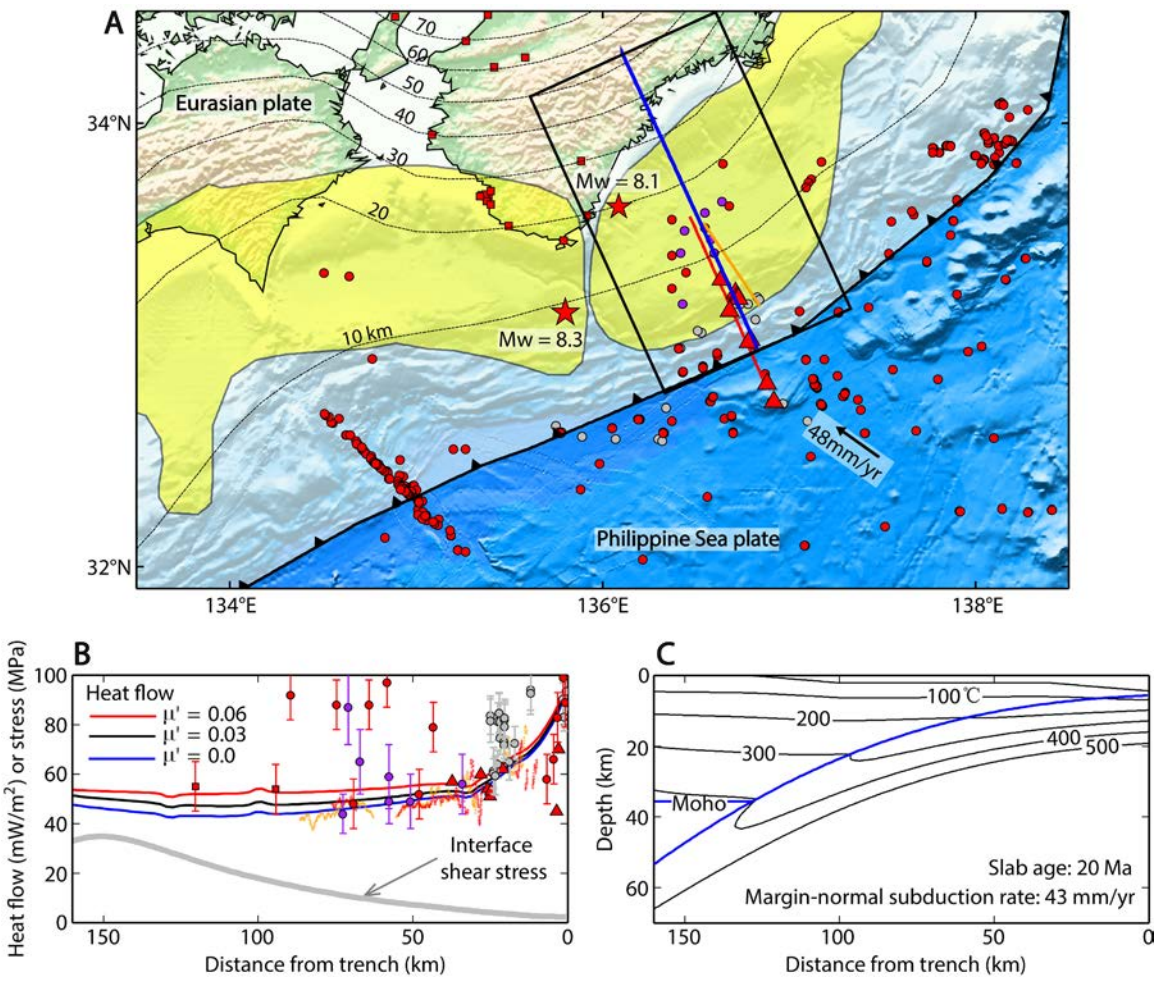

Fig. S3

Nankai model. (A) Tectonic setting. Red circles and squares indicate sites of marine probe and land borehole heat flow measurements, respectively, as compiled in (*69*). Purple and gray circles indicate sites of probe heat flow measurements with and without long-term temperature monitoring, respectively, reported by (*64*). Red triangles indicate IODP borehole sites (*49*, *67*). Thin red and orange lines represent seismic lines along which BSR heat flows were derived (*67*). Heat flow data shown in (B) are from the corridor (black box) along the model profile (thick blue line). Plate interface depths (black contours) are from (*33*). Yellow shading represents approximate rupture areas of the 1944 and 1946 M_w ~ 8.1-8.3 megathrust earthquakes (*84*) (Table S2). (B) Observed (symbol) and the model-predicted (lines) heat flows and model interface shear stress. Different types of heat flow measurements are shown using the same symbol and/or color coding as in (A). (C) Thermal structure. Interface geometry is constructed by using seismic survey data (*85*) for the shallower part and Slab 1.0 (*33*) for the deeper part.

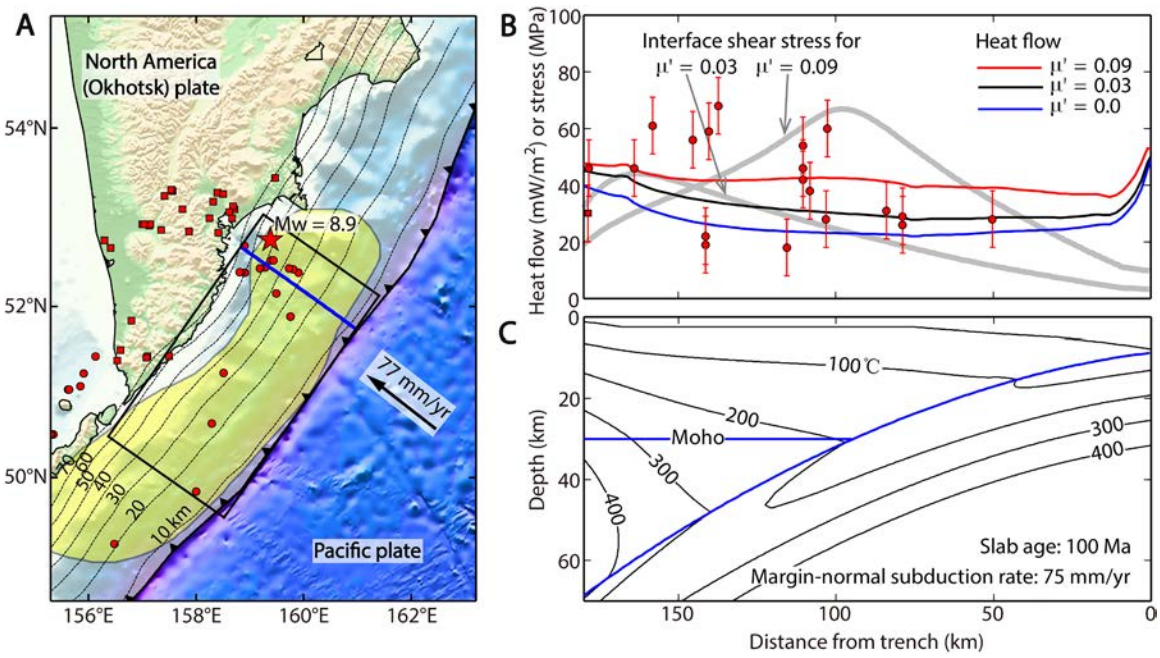

Fig. S4

Kamchatka model. (A) Tectonic setting. Red circles and squares indicate sites of marine probe and land borehole heat flow measurements, respectively, as compiled in (*69*). Heat flow data shown in (B) are from within the black box including the model profile (thick blue line). Plate interface depths (black contours) are from (*33*). Yellow shading represents rupture area of the 1952 M_w 8.9 earthquake (*86*) (Table S2), with epicenter shown with a red star. (B) Observed (symbols) and model-predicted (lines) surface heat flows and model interface shear stress. (C) Thermal structure. Interface geometry is the same as in (A).

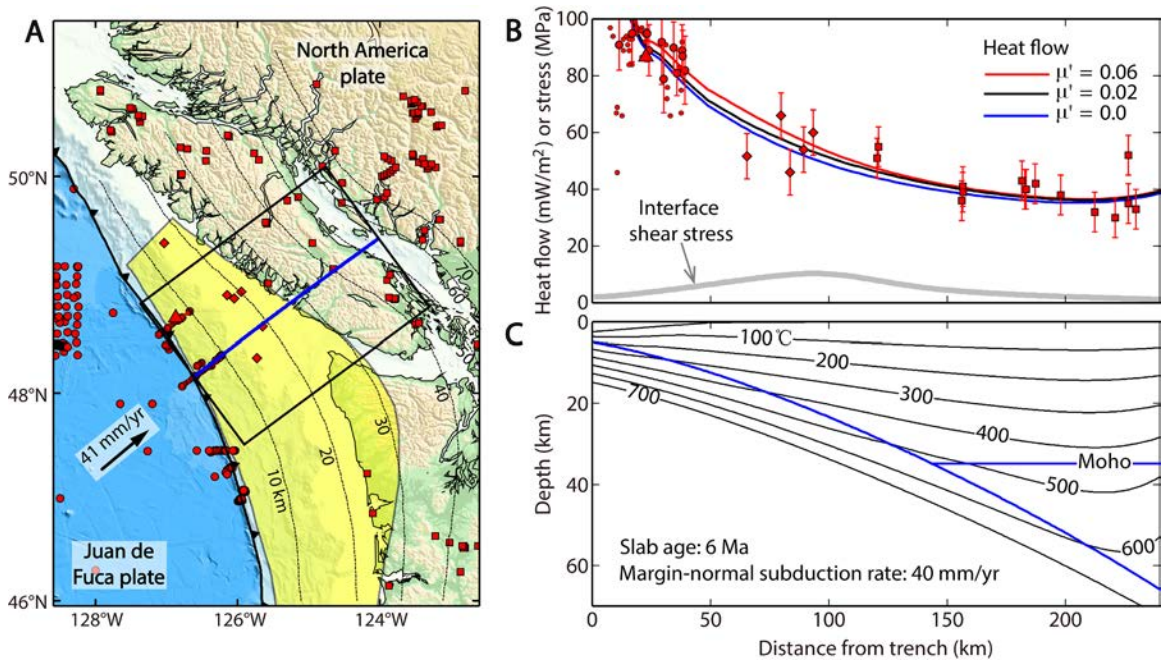

Fig. S5

Northern Cascadia model. (A) Tectonic setting. Red symbols indicate heat flow sites: small circles – BSR, larger circles – probes, diamonds – shelf wells, squares – land boreholes, triangle – ODP borehole. Heat flow data shown in (B) are from the corridor (black box) along the model profile (thick blue line). Plate interface depths (black contours) are from (*33*). Yellow shading represents the estimated rupture area of the AD 1700 Mw ~ 9.0 great earthquake (*87*) (Table S2). (B) Observed (symbol) and the model-predicted (lines) heat flow and model interface shear stress. Different types of heat flow measurements are shown using the same symbols as in (A). (C) Thermal structure. Interface geometry is constructed by using seismic reflection data (*70*) for the shallower part and Slab 1.0 (*33*) for the deeper part.

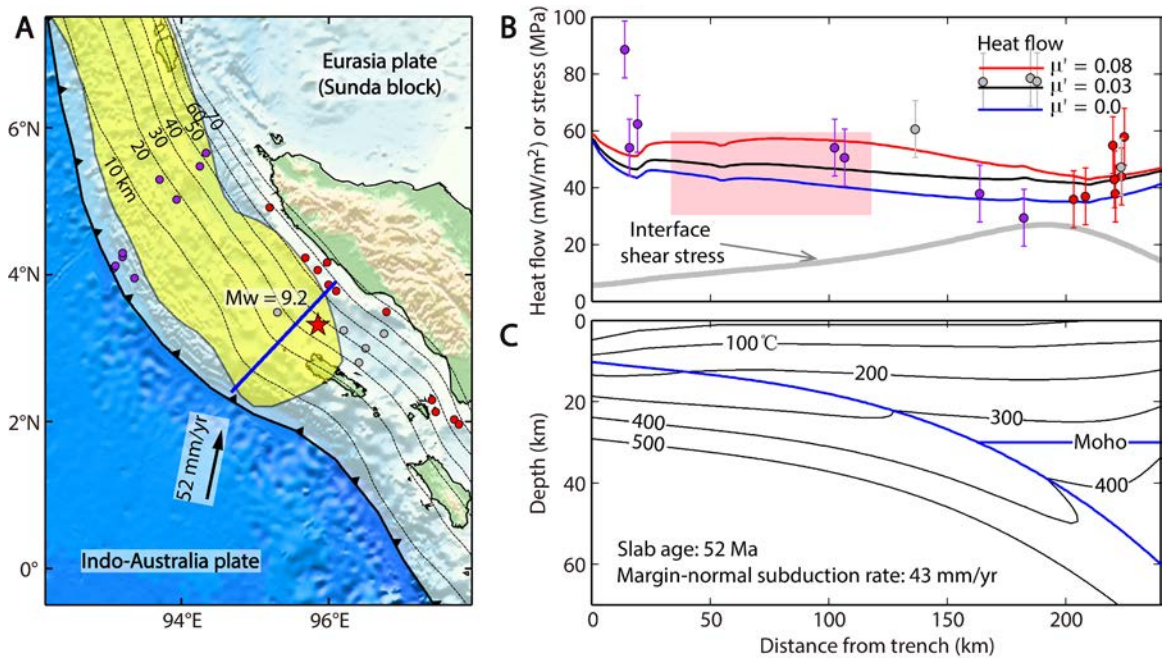

Fig. S6

Sumatra model. (A) Tectonic setting. Colors of probe heat flow sites (solid circles) indicate different sources: red – GHFD, purple – Marion Dufresne Flux data, grey – Sonne 189. Thick blue line indicates model profile. Plate interface depths (black contours) are from (*33*). Yellow shading represents rupture area of the 2004 Mw = 9.2 earthquake (*88*) (Table S2), with epicenter shown as red star. (B) Observed (symbols) and model-predicted (lines) heat flows and model interface shear stress. Different sources of probe heat flow data are shown using the same color coding as in (A). The range of the BSR heat flows (*76*) is roughly indicated using the pink shaded area (seismic lines not shown in (A)). (C) Thermal structure. Interface geometry is constructed by using seismic reflection data (*75*) for the shallower part and Slab 1.0 (*33*) for the deeper part.

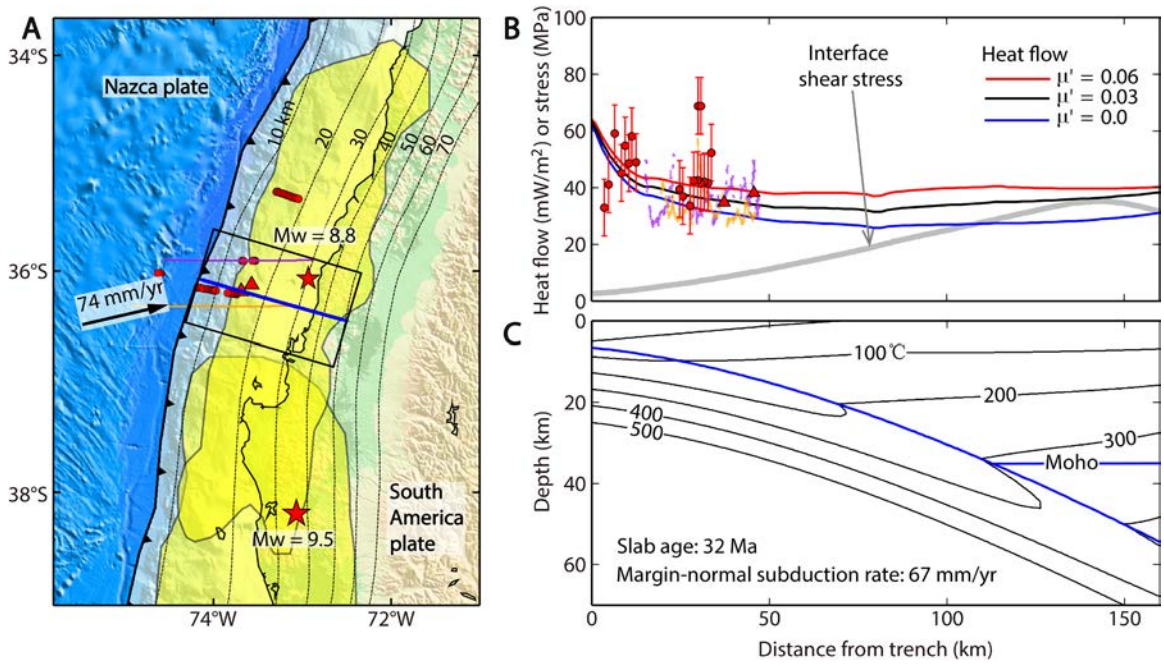

Fig. S7

South-Central Chile model. (A) Tectonic setting. Red circles indicate sites of probe heat flow measurements (*78, 79*). Red triangles indicate ODP borehole sites. Thin purple and orange lines represent seismic lines along which BSR heat flow data were derived (*43*). Heat flow data shown in (B) are from the corridor (black box) along the model profile (thick blue line). Plate interface depths (black contours) are from (*33*). Yellow shading represents rupture areas of the 1960 M_w 9.5 and 2010 M_w 8.8 earthquakes (*89*) (Table S2), with epicenters marked by red stars. (B) Observed (symbol) and the model-predicted (lines) heat flows and model interface shear stress. Different types of heat flow data are shown using the same symbol and/or color coding as in (A). (C) Thermal structure. Interface geometry is constructed by using seismic reflection data (*43*) for the shallower part and Slab 1.0 (*33*) for the deeper part.

Table S1.

Thermal Parameters Used in the Models

Thermal Unit	Thermal Conductivity ($W\ m^{-1}\ K^{-1}$)	Thermal Capacity ($MJ\ m^{-3}\ K^{-1}$)	Heat Production ($\mu W\ m^{-3}$)
Sediments	2.0	N/A[a]	0.2-1.7[b]
Continental upper crust	2.5	N/A[a]	0.2-1.8[b]
Continental lower curst	2.5	N/A[a]	0.4
Mantle wedge	3.1	3.3	0.02
Oceanic lithosphere	2.9	3.3	0.02

[a] Not required for steady-state modeling

[b] Values for different subduction zones are as described in “Model Parameters”

Table S2.

Summary of Subduction Zones Studied

Subduction zone	Maximum moment magnitude /Year	Predominant interseismic behavior	Smoothness of subducting seafloor	Sediment thickness on incoming plate (km)	Subduction azimuth (°) /rate (mm/yr)[a]	Model profile azimuth (°) /resolved rate (mm/yr)	Intersection of profile and trench [lon/lat (°)]	Preferred apparent friction μ'
N. Hikurangi	5.6 ± 0.5/1966 (*8*)	Creeping (*9*)	Extremely rough	< 1.0 (*103*)	293/45 (*9*)	293/45	178.6/-39.8	0.13
Manila Trench	6.3 ± 0.2[b]/2008 (*GCMT*)	Creeping (*96*)	Rough	1.5-2.0 (*104*)	121/93 (*38*)	80/70	120.2/20.6	0.09
Kermadec	8.1 ± 0.2[b]/1917 (*90*)	Unknown	Rough	< 0.25 (*105*)	273/62 (*38*)	286/60	-176.2/-29.3	0.07
Nankai	8.3/1946 (*91*)	Locking (*97*)	Smooth	1.5-2.0 (*67*)	305/48 (*107*)	331/43	136.8/33.0	0.03
Kamchatka	8.9 ± 0.1/1952 (*86*)	Locking (*98*)	Smooth	0.4-1.0 (*106*)	308/77 (*31*)	294/75	161.0/51.7	0.03
N. Cascadia	8.95 ± 0.25/1700 (*92*)	Locking (*99*)	Very smooth	2.0-3.0 (*70*)	50/40 (*38*)	63/40	-126.8/48.4	0.02
Japan Trench	9.0/2011 (*93*, *94*[c])	Locking (*100*)	Smooth	0.4-1.0 (*34*)	297/83 (*108*)	281/80	144.0/38.0	0.025
Sumatra	9.2 ± 0.1/2004 (*88*)	Locking (*101*)	Very smooth	4.0-5.0 (*75*)	10/52 (*109*)	44/43	94.7/2.4	0.03
S-C Chile	9.5/1960 (*95*)	Locking (*102*)	Very smooth	1.5-2.0 (*80*)	77/74 (*38*)	103/67	-74.1/-36.1	0.03

[a] Subduction rate is the motion of subducting plate relative to forearc region.

[b] Uncertainty is assumed to be 0.2.

[c] Rupture zone shown in Fig. 1.

References

1. C. H. Scholz, J. Campos, On the mechanism of seismic decoupling and back arc spreading at subduction zones. *J. Geophys. Res.* **100** (B11), 22,103–22,105 (1995). doi:10.1029/95JB01869

2. K. Wang, S. L. Bilek, Invited review paper: Fault creep caused by subduction of rough seafloor relief. *Tectonophys.* **610**, 1–24 (2014). doi:10.1016/j.tecto.2013.11.024

3. K. Wang, S. L. Bilek, Do subducting seamounts generate or stop large earthquakes? *Geology* **39**, 819–822 (2011). doi:10.1130/G31856.1

4. A. Heuret, C. P. Conrad, F. Funiciello, S. Lallemand, L. Sandri, Relation between subduction megathrust earthquakes, trench sediment thickness and upper plate strain. *Geophys. Res. Lett.* **39**, L05304 (2012). doi:10.1029/2011GL050712

5. D. W. Scholl, S. H. Kirby, R. von Huene, American Geophysical Union Fall Meeting, Abstract T14B–01 (2011).

6. Y. Yamanaka, M. Kikuchi, Asperity map along the subduction zone in northeastern Japan inferred from regional seismic data. *J. Geophys. Res.* **109**, B07307 (2004). doi:10.1029/2003JB002683

7. N. Uchida, T. Matsuzawa, Coupling coefficient, hierarchical structure, and earthquake cycle for the source area of the 2011 off the Pacific coast of Tohoku earthquake inferred from small repeating earthquake data. *Earth Planets Space* **63**, 675–679 (2011). doi:10.5047/eps.2011.07.006

8. T. Webb, H. Anderson, Focal mechanisms of large earthquakes in the North Island of New Zealand: Slip partitioning at an oblique active margin. *Geophys. J. Int.* **134**, 40–86 (1998). doi:10.1046/j.1365-246x.1998.00531.x

9. L. M. Wallace, M. Reyners, U. Cochran, S. Bannister, P. M. Barnes, K. Berryman, G. Downes, D. Eberhart-Phillips, A. Fagereng, S. Ellis, A. Nicol, R. McCaffrey, R. J. Beavan, S. Henrys, R. Sutherland, D. H. N. Barker, N. Litchfield, J. Townend, R. Robinson, R. Bell, K. Wilson, W. Power, Characterizing the seismogenic zone of a major plate boundary subduction thrust: Hikurangi Margin, New Zealand. *Geochem. Geophys. Geosyst.* **10**, Q10006 (2009). doi:10.1029/2009GC002610

10. D. H. N. Barker, R. Sutherland, S. Henrys, S. Bannister, Geometry of the Hikurangi subduction thrust and upper plate, North Island, New Zealand. *Geochem. Geophys. Geosyst.* **10**, Q02007 (2009). doi:10.1029/2008GC002153

11. Materials, methods, and other information are available as supplementary material on *Science* Online.

12. C. A. J. Wibberley, G. Yielding, G. Di Toro, in *The Internal Structure of Fault Zones: Implications for Mechanical and Fluid-Flow Properties*, Geol. Soc. Lond. Spec. Pub. 299, C. A. J. Wibberley, W. Kurz, J. Imber, R. E. Holdsworth, C. Collettini, Eds. (Geological Society of London, 2008), pp. 5–33.

13. H. Kanamori, L. Rivera, in *The missing sinks: Slip localization in faults, damage zones, and the seismic energy budget*, Geophys. Monogr. 170, Abercrombie, R., Ed. (America Geophysical Union, Washington DC, 2006), pp. 3–13.

14. H. Noda, T. Shimamoto, Transient behavior and stability analyses of halite shear zones with an empirical rate-and-state friction to flow law. *J. Struct. Geol.* **38**, 234–242 (2012). doi:10.1016/j.jsg.2011.08.012

15. J. Byerlee, Friction of rocks. *Pure Appl. Geophys.* **116**, 615–626 (1978). doi:10.1007/BF00876528

16. K. Wang, K. Suyehiro, How does plate coupling affect crustal stresses in northeast and southwest Japan? *Geophys. Res. Lett.* **26**, 2307–2310 (1999). doi:10.1029/1999GL900528

17. S. Lamb, Shear stresses on megathrusts: Implications for mountain building behind subduction zones. *J. Geophys. Res.* **111**, B07401 (2006). doi:10.1029/2005JB003916

18. Y. Kawada, M. Yamano, N. Seama, Hydrothermal heat mining in an incoming oceanic plate due to aquifer thickening: Explaining the high heat flow anomaly observed around the Japan Trench. *Geochem. Geophys. Geosyst.* **15**, 1580–1599 (2014). doi:10.1002/2014GC005285

19. G. Di Toro, R. Han, T. Hirose, N. De Paola, S. Nielsen, K. Mizoguchi, F. Ferri, M. Cocco, T. Shimamoto, Fault lubrication during earthquakes. *Nature* **471**, 494–498 (2011). Medline doi:10.1038/nature09838

20. B. P. Allmann, P. M. Shearer, Global variations of stress drop for moderate to large earthquakes. *J. Geophys. Res.* **114** (B1), B01310 (2009). doi:10.1029/2008JB005821

21. K. Koketsu, Y. Yokota, N. Nishimura, Y. Yagi, S. Miyazaki, K. Satake, Y. Fujii, H. Miyake, S. Sakai, Y. Yamanaka, T. Okada, A unified source model for the 2011 Tohoku earthquake. *Earth Planet. Sci. Lett.* **310**, 480–487 (2011). doi:10.1016/j.epsl.2011.09.009

22. S. J. Lee, B. S. Huang, M. Ando, H. C. Chiu, J. H. Wang, Evidence of large scale repeating slip during the 2011 Tohoku-Oki earthquake. *Geophys. Res. Lett.* **38**, L19306 (2011). doi:10.1029/2011GL049580

23. H. Kumagai, N. Pulido, E. Fukuyama, S. Aoi, Strong localized asperity of the 2011 Tohoku-Oki earthquake. *Earth Planets Space* **64**, 649–654 (2012). doi:10.5047/eps.2012.01.004

24. In some earthquakes, the final fault stress at the end of the rupture may be somewhat smaller (overshoot) or larger (undershoot) than the fault strength during slip, but the deviation from the coseismic strength is expected to be a small fraction of the stress drop.

25. A. Hasegawa, K. Yoshida, Y. Asano, T. Okada, T. Iinuma, Y. Ito, Change in stress field after the 2011 great Tohoku-Oki earthquake. *Earth Planet. Sci. Lett.* **355-356**, 231–243 (2012). doi:10.1016/j.epsl.2012.08.042

26. M. E. Pritchard, M. Simons, An aseismic slip pulse in northern Chile and along-strike variations in seismogenic behavior. *J. Geophys. Res.* **111**, B08405 (2006). 10.1029/2006JB004258

27. R. E. Abercrombie, J. R. Rice, Can observations of earthquake scaling constrain slip weakening? *Geophys. J. Int.* **162**, 406–424 (2005). doi:10.1111/j.1365-246X.2005.02579.x

28. D. A. Lockner, C. Morrow, D. Moore, S. Hickman, Low strength of deep San Andreas fault gouge from SAFOD core. *Nature* **472**, 82–85 (2011). Medline doi:10.1038/nature09927

29. D. I. Doser, T. H. Webb, Source parameters of large historical (1917-1961) earthquakes, North Island, New Zealand. *Geophys. J. Int.* **152**, 795–832 (2003). doi:10.1046/j.1365-246X.2003.01895.x

30. W. Power, L. Wallace, X. Wang, M. Reyners, Tsunami Hazard Posed to New Zealand by the Kermadec and Southern New Hebrides Subduction Margins: An Assessment Based on Plate Boundary Kinematics, Interseismic Coupling, and Historical Seismicity. *Pure Appl. Geophys.* **169**, 1–36 (2012). doi:10.1007/s00024-011-0299-x

31. I. Wada, K. Wang, Common depth of slab-mantle decoupling: Reconciling diversity and uniformity of subduction zones. *Geochem. Geophys. Geosyst.* **10**, 10009 (2009). doi:10.1029/2009GC002570

32. P. E. van Keken, B. Kiefer, S. M. Peacock, High-resolution models of subduction zones: Implications for mineral dehydration reactions and the transport of water into the deep mantle. *Geochem. Geophys. Geosyst.* **3**, 1056 (2002). doi:10.1029/2001GC000256

33. G. P. Hayes, D. J. Wald, R. L. Johnson, Slab1.0: A three-dimensional model of global subduction zone geometries. *J. Geophys. Res.* **117** (B1), B01302 (2012). doi:10.1029/2011JB008524

34. T. Tsuji, K. Kawamura, T. Kanamatsu, T. Kasaya, K. Fujikura, Y. Ito, T. Tsuru, M. Kinoshita, Extension of continental crust by anelastic deformation during the 2011 Tohoku-oki earthquake: The role of extensional faulting in the generation of a great tsunami. *Earth Planet. Sci. Lett.* **364**, 44–58 (2013). doi:10.1016/j.epsl.2012.12.038

35. J. H. Ansell, S. C. Bannister, Shallow morphology of the subducted Pacific plate along the Hikurangi margin, New Zealand. *Phys. Earth Planet. Inter.* **93**, 3–20 (1996). doi:10.1016/0031-9201(95)03085-9

36. C. A. Stein, S. Stein, A model for the global variation in oceanic depth and heat flow with lithospheric age. *Nature* **359**, 123–129 (1992). doi:10.1038/359123a0

37. S. Kodaira, T. Sato, N. Takahashi, A. Ito, Y. Tamura, Y. Tatsumi, Y. Kaneda, Seismological evidence for variable growth of crust along the Izu intraoceanic arc. *J. Geophys. Res.* **112** (B5), B05104 (2007). doi:10.1029/2006JB004593

38. C. DeMets, R. G. Gordon, D. F. Argus, Geologically current plate motions. *Geophys. J. Int.* **181**, 1–80 (2010). doi:10.1111/j.1365-246X.2009.04491.x

39. Y. Miyake, Y. Sugimura, Y. Hirao, Uranium, thorium, and potassium contents in granitic and basaltic rocks in Japan. in *The Natural Radiation Environment II*, 535-558 (1975).

40. R. D. Hyndman, K. Wang, M. Yamano, Thermal constraints on the seismogenic portion of the southwestern Japan subduction thrust. *J. Geophys. Res.* **100** (B8), 15373–15392 (1995). doi:10.1029/95JB00153

41. T. I. Yamaguchi, M. Yamano, T. Nagao, S. Goto, Distribution of radioactive heat production around an active fault and in accretionary prisms of southwest Japan. *Phys. Earth Planet. Inter.* **126**, 269–277 (2001). doi:10.1016/S0031-9201(01)00260-6

42. O. P. Pandey, Terrestrial heat flow in New Zealand. Ph. D. thesis, Victoria University of Wellington, New Zealand (1981).

43. I. Grevemeyer, J. L. Diaz-Naveas, C. R. Ranero, H. Villinger, Ocean Drilling Program Leg 202 Scientific Party, Heat flow over the descending Nazca plate in Central Chile, 32°S to 41°S: Observations from ODP Leg 202 and the occurrence of natural gas hydrates. *Earth Planet. Sci. Lett.* **213**, 285–298 (2003). doi:10.1016/S0012-821X(03)00303-0

44. T. J. Lewis, W. H. Bentkowski, E. E. Davis, R. D. Hyndman, J. A. Wright, Subduction of the Juan de Fuca plate: Thermal consequences. *J. Geophys. Res.* **93** (B12), 15207–15225 (1988). doi:10.1029/JB093iB12p15207

45. K. Wang, T. Mulder, G. C. Rogers, R. D. Hyndman, Case for very low coupling stress on the cascadia subduction fault. *J. Geophys. Res.* **100** (B7), 12907–12918 (1995). doi:10.1029/95JB00516

46. I. Wada, K. Wang, J. He, R. D. Hyndman, Weakening of the subduction interface and its effects on surface heat flow, slab dehydration, and mantle wedge serpentinization. *J. Geophys. Res.* **113** (B4), B04402 (2008). doi:10.1029/2007JB005190

47. S. H. Bloomer, A. Ewart, J. M. Hergt, W. B. Bryan, Geochemistry and origin of igneous rocks from the outer Tonga forearc (Sit841). *Proc. Ocean Drill. Program, Sci. Results* **135**, 625–646 (1994).

48. G. A. Spinelli, K. Wang, Effects of fluid circulation in subducting crust on Nankai margin seismogenic zone temperatures. *Geology* **36**, 887–890 (2008). doi:10.1130/G25145A.1

49. R. Harris, M. Yamano, M. Kinoshita, G. Spinelli, H. Hamamoto, J. Ashi, A synthesis of heat flow determinations and thermal modeling along the Nankai Trough, Japan. *J. Geophys. Res.* **118**, 2687–2702 (2013). doi:10.1002/jgrb.50230

50. F. D. Hansen, N. L. Carter, Semibrittle creep of dry and wet Westerly granite at 1000 MPa. *U. S. Symp. on Rock Mechanics, 24th*, 429–447 (Texas A & M. Univ., College Station, Texas, 1983).

51. M. G. Langseth, E. A. Silver, The Nicoya convergent margin: A region of exceptionally low heat flow. *Geophys. Res. Lett.* **23**, 891–894 (1996). doi:10.1029/96GL00733

52. R. N. Harris, K. Wang, Thermal models of the Middle America Trench at the Nicoya Peninsula, Costa Rica. *Geophys. Res. Lett.* **29**, 2010 (2002). doi:10.1029/2002GL015406

53. R. N. Harris, G. Spinelli, C. R. Ranero, I. Grevemeyer, H. Villinger, U. Barckhausen, Thermal regime of the Costa Rican convergent margin: 2. Thermal models of the shallow Middle America subduction zone offshore Costa Rica. *Geochem. Geophys. Geosyst.* **11**, Q12S29 (2010). doi:10.1029/2010GC003273

54. J. Townend, Estimates of conductive heat flow through bottom-simulating reflectors on the Hikurangi and southwest Fiordland continental margins, *New Zealand*. *Mar. Geol.* **141**, 209–220 (1997). doi:10.1016/S0025-3227(97)00073-X

55. B. D. Field *et al*., Eds., *Cretaceous-Cenozoic geology and Petroleum Systems of the East Coast Region, New Zealand* (Institute of Geological and Nuclear Sciences, Lower Hutt, New Zealand, 1997), vol.19 of *Institute of Geological and Nuclear Sciences Monograph*.

56. F. E. Studt, G. E. K. Thompson, Geothermal heat flow in the North Island of New Zealand. *N.Z. J. Geol. Geophys.* **12**, 673–683 (1969). doi:10.1080/00288306.1969.10431105

57. R. McCaffrey, L. M. Wallace, J. Beavan, Slow slip and frictional transition at low temperature at the Hikurangi subduction zone. *Nat. Geosci.* **1**, 316–320 (2008). doi:10.1038/ngeo178

58. A. Fagereng, S. Ellis, On factors controlling the depth of interseismic coupling on the Hikurangi subduction interface, New Zealand. *Earth Planet. Sci. Lett.* **278**, 120–130 (2009). doi:10.1016/j.epsl.2008.11.033

59. P. Molnar, P. England, Temperature heat flux, and frictional stress near major thrust faults. *J. Geophys. Res.* **95** (B4), 4833–4856 (1990). doi:10.1029/JB095iB04p04833

60. W. C. Chi, D. L. Reed, Evolution of shallow, crustal thermal structure from subduction to collision: An example from Taiwan. *Geol. Soc. Am. Bull.* **120**, 679–690 (2008). doi:10.1130/B26210.1

61. C. T. Shyu, S. K. Hsu, C. S. Liu, Heat flows off southwest Taiwan: Measurements over mud diapirs and estimated from bottom simulating reflectors. *Terr. Atmos. Ocean. Sci.* **9**, 795–812 (1998).

62. C. T. Shyu, Y. J. Chen, S. T. Chiang, C. S. Liu, Heat flow measurements over bottom simulating reflectors offshore southwestern Taiwan. *Terr. Atmos. Ocean. Sci.* **17**, 845 (2006).

63. R. Von Herzen, C. Ruppel, P. Molnar, M. Nettles, S. Nagihara, G. Ekström, A constraint on the shear stress at the Pacific-Australian plate boundary from heat flow and seismicity at the Kermadec forearc. *J. Geophys. Res.* **106** (B4), 6817–6833 (2001). doi:10.1029/2000JB900469

64. H. Hamamoto, M. Yamano, S. Goto, M. Kinoshita, K. Fujino, K. Wang, Heat flow distribution and thermal structure of the Nankai subduction zone off the Kii Peninsula. *Geochem. Geophys. Geosyst.* **12**, Q0AD20 (2011). doi:10.1029/2011GC003623

65. K. Wang, R. D. Hyndman, M. Yamano, Thermal regime of the southwest Japan subduction zone: Effects of age history of the subducting plate. *Tectonophys.* **248**, 53–69 (1995). doi:10.1016/0040-1951(95)00028-L

66. S. M. Peacock, K. Wang, Seismic consequences of warm versus cool subduction metamorphism: Examples from southwest and northeast japan. *Science* **286**, 937–939 (1999). Medline doi:10.1126/science.286.5441.937

67. B. Marcaillou, P. Henry, M. Kinoshita, T. Kanamatsu, E. Screaton, H. Daigle, V. Harcouët-Menou, Y. Lee, O. Matsubayashi, M. Kyaw Thu, S. Kodaira, M. Yamano, Seismogenic zone temperatures and heat-flow anomalies in the Tonankai margin segment based on temperature data from IODP expedition 333 and thermal model. *Earth Planet. Sci. Lett.* **349–350**, 171–185 (2012). doi:10.1016/j.epsl.2012.06.048

68. S. Yoshioka, Y. Suminokura, T. Matsumoto, J. Nakajima, Two-dimensional thermal modeling of subduction of the Philippine Sea Plate beneath southwest Japan. *Tectonophys.* **608**, 1094–1108 (2013). doi:10.1016/j.tecto.2013.07.003

69. A. Tanaka, M. Yamano, Y. Yano, M. Sasada, Geothermal gradient and heat flow data in and around Japan (I): Appraisal of heat flow geothermal gradient data. *Earth Planets Space* **56**, 1191–1194 (2004).

70. E. E. Davis, R. D. Hyndman, H. Villinger, Rates of fluid expulsion across the northern Cascadia accretionary prism constraints from new heat flow and multichannel seismic reflection data. *J. Geophys. Res.* **95** (B6), 8869–8889 (1990). doi:10.1029/JB095iB06p08869

71. R. D. Hyndman, K. Wang, T. Yuan, G. D. Spence, Tectonic sediment thickening, fluid expulsion, and the thermal regime of subduction zone accretionary prisms: The Cascadia margin off Vancouver Island. *J. Geophys. Res.* **98** (B12), 21865–21876 (1993). doi:10.1029/93JB02391

72. R. D. Hyndman, K. Wang, Thermal constraints on the zone of major thrust earthquake failure: The Cascadia subduction zone. *J. Geophys. Res.* **98** (B2), 2039–2060 (1993). doi:10.1029/92JB02279

73. Y. Furukawa, S. Uyeda, Thermal state under the Tohoko Arc with consideration of crustal heat generation. *Tectonophys.* **164**, 175–187 (1989). doi:10.1016/0040-1951(89)90011-5

74. G. Kimura, S. Hina, Y. Hamada, J. Kameda, T. Tsuji, M. Kinoshita, A. Yamaguchi, Runaway slip to the trench due to rupture of highly pressurized megathrust beneath the middle trench slope: The tsunamigenesis of the 2011 Tohoku earthquake off the east coast of northern Japan. *Earth Planet. Sci. Lett.* **339-340**, 32–45 (2012). doi:10.1016/j.epsl.2012.04.002

75. F. Klingelhoefer, M.-A. Gutscher, S. Ladage, J.-X. Dessa, D. Graindorge, D. Franke, C. André, H. Permana, T. Yudistira, A. Chauhan, Limits of the seismogenic zone in the epicentral region of the 26 December 2004 great Sumatra-Andaman earthquake: Results from seismic refraction and wide-angle reflection surveys and thermal modeling. *J. Geophys. Res.* **115** (B1), B01304 (2010). doi:10.1029/2009JB006569

76. G. Delisle, M. Zeibig, Marine heat flow measurements in hard ground offshore Sumatra. *Eos Trans. AGU* **88**, 38–39 (2007). doi:10.1029/2007EO040004

77. S. Hippchen, R. D. Hyndman, Thermal and structural models of the Sumatra subduction zone: Implications for the megathrust seismogenic zone. *J. Geophys. Res.* **113** (B12), B12103 (2008). doi:10.1029/2008JB005698

78. I. Grevemeyer, N. Kaul, J. L. Diaz-Naveas, H. W. Villinger, C. R. Ranero, C. Reichert, Heat flow and bending-related faulting at subduction trenches: Case studies offshore of Nicaragua and Central Chile. *Earth Planet. Sci. Lett.* **236**, 238–248 (2005). doi:10.1016/j.epsl.2005.04.048

79. I. Grevemeyer, N. Kaul, J. L. Diaz-Naveas, Geothermal evidence for fluid flow through the gas hydrate stability field off Central Chile - transient flow related to large subduction

zone earthquakes? *Geophys. J. Int.* **166**, 461–468 (2006). doi:10.1111/j.1365-246X.2006.02940.x

80. D. Völker, I. Grevemeyer, M. Stipp, K. Wang, J. He, Thermal control of the seismogenic zone of southern central Chile. *J. Geophys. Res.* **116** (B10), B10305 (2011). doi:10.1029/2011JB008247

81. K. Mclntosh, H. van Avendonk, L. Lavier, W. R. Lester, D. Eakin, F. Wu, C.-S. Liu, C.-S. Lee, Inversion of a hyper-extended rifted margin in the southern Central Range of Taiwan. *Geology* **41**, 871–874 (2013). doi:10.1130/G34402.1

82. W. C. Chi, D. L. Reed, G. Moore, T. Nguyen, C.-S. Liu, N. Lundberg, Tectonic wedging along the rear of offshore Taiwan accretionary prism. *Tectonophys.* **374**, 199–217 (2003). doi:10.1016/j.tecto.2003.08.004

83. B. C. Bautista, M. L.-P. Bautista, K. Oike, F. T. Wu, R. S. Punongbayan, A new insight on the geometry of subducting slabs in northern Luzon, Philippines. *Tectonophys.* **339**, 279–310 (2001). doi:10.1016/S0040-1951(01)00120-2

84. T. Baba, P. R. Cummins, Contiguous rupture areas of two Nankai Trough earthquakes revealed by high-resolution tsunami waveform inversion. *Geophys. Res. Lett.* **32**, L08305 (2005). doi:10.1029/2004GL022320

85. J. O. Park, T. Tsuru, S. Kodaira, P. R. Cummins, Y. Kaneda, Splay fault branching along the Nankai subduction zone. *Science* **297**, 1157–1160 (2002). Medline doi:10.1126/science.1074111

86. B. T. MacInnes, R. Weiss, J. Bourgeois, T. K. Pinegina, Slip distribution of the 1952 Kamchatka great earthquake based on near-field tsunami deposits and historical records. *Bull. Seismol. Soc. Am.* **100**, 1695–1709 (2010). doi:10.1785/0120090376

87. P. Wang, S. E. Engelhart, K. Wang, A. D. Hawkes, B. P. Horton, A. R. Nelson, R. C. Witter, Heterogeneous rupture in the great Cascadia earthquake of 1700 inferred from coastal subsidence estimates. *J. Geophys. Res.* **118**, 2460–2473 (2013). doi:10.1002/jgrb.50101

88. T. Lay, H. Kanamori, C. J. Ammon, M. Nettles, S. N. Ward, R. C. Aster, S. L. Beck, S. L. Bilek, M. R. Brudzinski, R. Butler, H. R. DeShon, G. Ekström, K. Satake, S. Sipkin, The great Sumatra-Andaman earthquake of 26 December 2004. *Science* **308**, 1127–1133 (2005). Medline doi:10.1126/science.1112250

89. M. S. Moreno, J. Bolte, J. Klotz, D. Melnick, Impact of megathrust geometry on inversion of coseismic slip from geodetic data: Application to the 1960 Chile earthquake. *Geophys. Res. Lett.* **36**, L16310 (2009). doi:10.1029/2009GL039276

90. W. Power, L. Wallace, X. Wang, M. Reyners, Tsunami hazard posed to New Zealand by the Kermadec and southern New Hebrides subduction margins: An assessment based on plate boundary kinematics, interseismic coupling, and historical seismicity. *Pure Appl. Geophys.* **169**, 1–36 (2012). doi:10.1007/s00024-011-0299-x

91. H. Kanamori, Tectonic implications of the 1944 Tonankai and 1946 Nankaido earthquakes. *Phys. Earth Planet. Inter.* **5**, 129–139 (1972). doi:10.1016/0031-9201(72)90082-9

92. K. Satake, K. Wang, B. F. Atwater, Fault slip and seismic moment of the 1700 Cascadia earthquake inferred from Japanese tsunami descriptions. *J. Geophys. Res.* **108** (B11), 2535 (2003). doi:10.1029/2003JB002521

93. S. Ide, A. Baltay, G. C. Beroza, Shallow dynamic overshoot and energetic deep rupture in the 2011 Mw 9.0 Tohoku-Oki earthquake. *Science* **332**, 1426–1429 (2011). Medline doi:10.1126/science.1207020

94. G. Shao, J. Chen, R. Archuleta, Quality of earthquake source models constrained by teleseismic waves: Using the 2011 M9 Tohoku-oki earthquake as an example. Incorporated Research Institutions for Seismology Workshop, Poster 93, Boise, Idaho, June 13–15 (2012).

95. G. Plafker, J. C. Savage, Mechanism of the Chilean earthquakes of May 21 and 22, 1960. *Geol. Soc. Am. Bull.* **81**, 1001–1030 (1970). doi:10.1130/0016-7606(1970)81[1001:MOTCEO]2.0.CO;2

96. G. Galgana, M. Hamburger, R. McCaffrey, E. Corpuz, Q. Chen, Analysis of crustal deformation in Luzon, Philippines using geodetic observations and earthquake focal mechanisms. *Tectonophys.* **432**, 63–87 (2007). doi:10.1016/j.tecto.2006.12.001

97. S. Yoshioka, Y. Matsuoka, Interplate coupling along the Nankai Trough, southwest Japan, inferred from inversion analyses of GPS data: Effects of subducting plate geometry and spacing of hypothetical ocean-bottom GPS stations. *Tectonophys.* **600**, 165–174 (2013). doi:10.1016/j.tecto.2013.01.023

98. R. Bürgmann, M. G. Kogan, G. M. Steblov, G. Hilley, V. E. Levin, E. Apel, Interseismic coupling and asperity distribution along the Kamchatka subduction zone. *J. Geophys. Res.* **110**, B07405 (2005). doi:10.1029/2005JB003648

99. S. Mazzotti, H. Dragert, J. Henton, M. Schmidt, R. Hyndman, T. James, Y. Lu, M. Craymer, Current tectonics of northern Cascadia from a decade of GPS measurements. *J. Geophys. Res.* **108**, 2554 (2003). doi:10.1029/2003JB002653

100. Y. Suwa, S. Miura, A. Hasegawa, T. Sato, K. Tachibana, Interplate coupling beneath NE Japan inferred from three-dimensional displacement field. *J. Geophys. Res.* **111** (B4), B04402 (2006). doi:10.1029/2004JB003203

101. L. Prawirodirdjo, R. McCaffrey, C. D. Chadwell, Y. Bock, C. Subarya, Geodetic observations of an earthquake cycle at the Sumatra subduction zone: Role of interseismic strain segmentation. *J. Geophys. Res.* **115** (B3), B03414 (2010). doi:10.1029/2008JB006139

102. M. Métois, A. Socquet, C. Vigny, Interseismic coupling, segmentation and mechanical behavior of the central Chile subduction zone. *J. Geophys. Res.* **117** (B3), B03406 (2012). doi:10.1029/2011JB008736

103. K. B. Lewis, J.-Y. Collot, S. E. Lallem, The dammed Hikurangi Trough: A channel-fed trench blocked by subducting seamounts and their wake avalanches (New Zealand–France GeodyNZ Project). *Basin Res.* **10**, 441–468 (1998). doi:10.1046/j.1365-2117.1998.00080.x

104. F. Li, Z. Sun, D. Hu, Z. Wang, Crustal structure and deformation associated with seamount subduction at the north Manila trench represented by analog and gravity modeling. *Mar. Geophys. Res.* **34**, 393–406 (2013). doi:10.1007/s11001-013-9193-5

105. J. Whittaker, A. Goncharov, S. Williams, R. D. Müller, G. Leitchenkov, Global sediment thickness data set updated for the Australian-Antarctic Southern Ocean. *Geochem. Geophys. Geosyst.* **14**, 3297–3305 (2013). doi:10.1002/ggge.20181

106. H. Gnibidenko *et al*., The Tectonics of the Kuril-Kamchatka deep-sea trench, in *Geodynamics of the Western Pacific-Indonesian Region*, T. W. C. Hilde, S. Uyeda, Eds., (AGU, Washington DC, ed. 1, 1991), vol. 11 of *Geodynamics Series*, pp. 249–285.

107. J. P. Loveless, B. J. Meade, Geodetic imaging of plate motions, slip rates, and partitioning of deformation in Japan. *J. Geophys. Res.* **115** (B2), B02410 (2010). doi:10.1029/2008JB006248

108. Z. Altamimi, X. Collilieux, J. Legrand, B. Garayt, C. Boucher, ITRF2005: A new release of the International Terrestrial Reference Frame based on time series of station positions and Earth orientation parameters. *J. Geophys. Res.* **112** (B9), B09401 (2007). doi:10.1029/2007JB004949

109. K. Sieh, D. Natawidjaja, Neotectonics of the Sumatran fault, Indonesia. *J. Geophys. Res.* **105** (B12), 28295–28326 (2000). doi:10.1029/2000JB900120